# Functional Rotation Induced by Alternating Protonation States in the Multidrug Transporter AcrB: All-Atom Molecular Dynamics Simulations

Tsutomu Yamane,[†] Satoshi Murakami,[‡] and Mitsunori Ikeguchi*,[†]

[†]Graduate School of Medical Life Science, Yokohama City University, 1-7-29 Suehiro-cho, Tsurumi-ku, Yokohama 230-0045, Japan

[‡]Graduate School of Bioscience & Biotechnology, Tokyo Institute of Technology, 4259, Nagatsuda-cho, Midori-ku, Yokohama 226-8501, Japan

Ⓢ *Supporting Information*
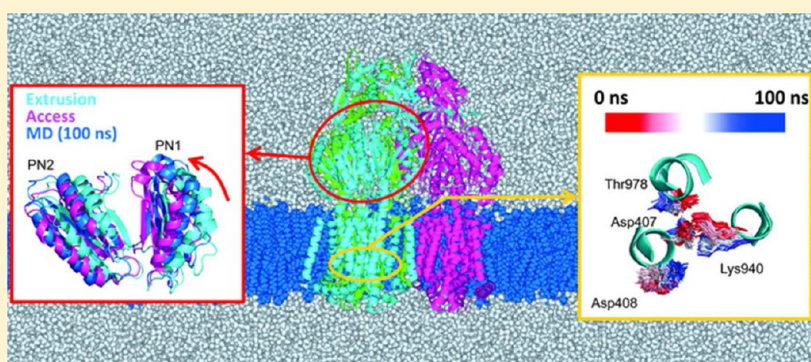
ABSTRACT: The multidrug transporter AcrB actively exports a wide variety of noxious compounds using proton-motive force as an energy source in Gram-negative bacteria. AcrB adopts an asymmetric structure comprising three protomers with different conformations that are sequentially converted during drug export; these cyclic conformational changes during drug export are referred to as functional rotation. To investigate functional rotation driven by proton-motive force, all-atom molecular dynamics simulations were performed. Using different protonation states for the titratable residues in the middle of the transmembrane domain, our simulations revealed the correlation between the specific protonation states and the side-chain configurations. Changing the protonation state for Asp408 induced a spontaneous structural transition, which suggests that the proton translocation stoichiometry may be one proton per functional rotation cycle. Furthermore, our simulations demonstrate that alternating the protonation states in the transmembrane domain induces functional rotation in the porter domain, which is primarily responsible for drug transport.

Bacterial multidrug resistance is an increasing threat to treating infectious diseases. A key basis for bacteria multidrug resistance is the expression of multidrug efflux transporters, which export drugs out of cells.[1] Acriflavine resistance protein B (AcrB) and its homologues are resistance, nodulation, and cell division (RND) transporters, which are the major multidrug efflux transporters for Gram-negative bacteria and confer intrinsic drug tolerance and multidrug resistance when they are overproduced.[2−5] AcrB cooperates with an outer-membrane channel, TolC, and a membrane fusion protein, AcrA.[6−9] This tripartite complex exports many antibiotics, antiseptics, anticancer chemotherapeutics, and toxic compounds, including anionic, cationic, zwitterionic, and neutral compounds, directly out of the cells through proton-motive force.[10,11]

Although the full structure for the AcrA-AcrB-TolC complex has not been solved, the individual component structures have been determined.[12−14] Among such components, AcrB is a key component that determines substrate specificity and actively exports substrates.[15] Its first crystal structure was solved in 2002.[16] Notably, AcrB was the first secondary-active transporter structure solved at high resolution.[17] The structure revealed that AcrB is a homotrimer with a triangular-prism shape, and each protomer comprises three domains: the transmembrane (TM), porter, and TolC docking domains (Figure 1).[18] The TM domain transfers protons across the inner membrane and collects the driving energy. The translocation pathway for drugs is in the porter domain, which comprises four subdomains: PN1, PN2, PC1, and PC2. Subsequent X-ray studies in 2006 and 2007 showed that the AcrB structure is asymmetric among the three protomers;[19−21] each protomer has a different conformation that represents one of the three functional states in the substrate transport cycle: access (A), binding (B), and extrusion (E) (loose, tight, and open in other studies,
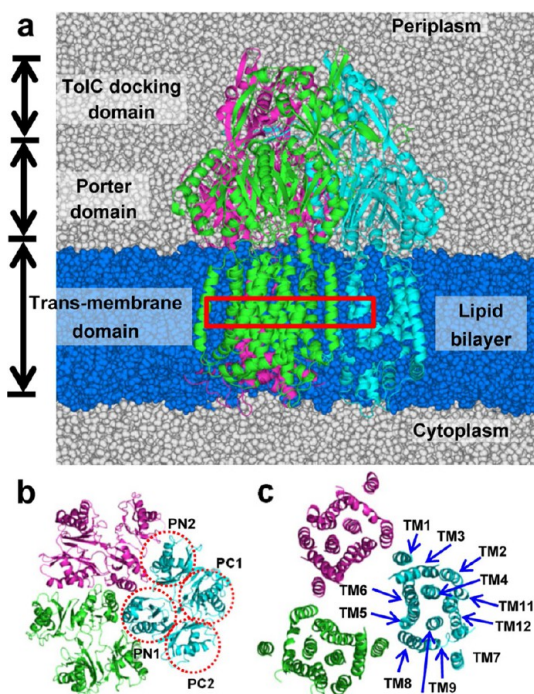
Figure 1. Snapshot of the simulation system. AcrB protomers A, B, and E are green, cyan and magenta, respectively. The lipid bilayer membrane is blue, and the water molecules are gray spheres.

respectively).[20,21] In protomer A, substrates can access the vestibule proximal to the aromatic-binding-pocket entrance in the porter domain; in protomer B, a substrate is bound inside the binding pocket. In protomer E, the vestibule is closed, and the pocket exit to the outside of the cell through TolC is open. This asymmetric structure indicates that drugs are exported through a three-step functionally rotating mechanism, wherein protomers undergo sequential conformational changes from state A to B then to E and back to A.[19−21]

The alternating access mechanism was originally proposed in 1966, wherein the accessible gates change for the porter-domain binding pocket in the asymmetric structure (i.e., the protomers A and B open vestibules and the protomer E opens exit).[22] This process has been investigated through structural and functional studies on multiple transporters over the past decade as a key mechanism for active transport across membranes.[23−25] In contrast to most other transporters, wherein the TM domain is the site for alternating substrate access, the porter domain in the periplasmic space facilitates such alternating access for the RND transporter.[26] Therefore, the substrate translocation pathway is spatially separate from the sites that transduce energy from proton-motive force in the TM domain. Substrate translocation and energy transduction are also spatially separated in ABC transporters. In these transporters, machinery that transmits energy between the two distant sites is required for active transport. Successive conformational changes from the TM domain to the porter domain are likely involved in the RND transporter machinery. Thus, the TM domain conformational changes induced by proton translocation are a crucial initial step for drug efflux in the RND transporters.

The middle of the TM domain includes three titratable residues, Asp407, Asp408, and Lys940, which are functionally essential based on site-directed mutagenesis studies using MexB

and AcrB.[27,28] When these residues are replaced with any other amino-acid residues, the mutants entirely lose drug resistance.[27,28] These residues are important to the proton translocation pathway across membranes.[29,30] In crystal structures, these residues are in the middle of α-helices TM4 and TM10 (Asp407 and Asp408 in TM4; Lys940 in TM10), and in the asymmetric structure, the relative side-chain arrangements differ among the three protomers; Lys940 is located between Asp407 and Asp408 in protomers A and B and between Asp408 and Thr978 in protomer E (Figure 2). The
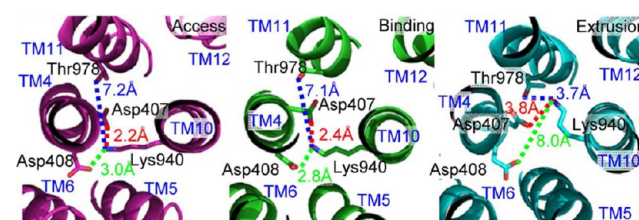

Figure 2. Side-chain configurations for three titratable residues in the transmembrane domain for protomers A (access), B (binding), and E (extrusion).

conformation difference is likely due to the titratable-group protonation states in these residues. However, the correlation between the specific protonation state and side-chain configurations remains unclear, even though such conformational changes are critical to harnessing proton-motive force.

Observing protons experimentally remains a challenging task for protein X-ray crystallography, especially for macromolecules, even where the resolution is better than 1.0 Å. Although the best resolution for the available AcrB crystal structures is ~1.9 Å,[31] it is difficult to observe hydrogen atoms through X-ray crystallography. Therefore, computational approaches, such as molecular dynamics (MD) simulations, are complementary.

Previous computational studies for AcrB have focused on conformational cycling and drug transport using all-atom targeted molecular dynamics simulations,[32−34] water pathways in the TM domain,[30] porter-domain motions,[35,36] drug binding in the porter domain,[37,38] structural transitions for the isolated porter domains using coarse-grained simulations,[39] and overall flexibility through normal-mode analysis with elastic-network models.[40] Here, we report using unbiased all-atom AcrB molecular dynamics simulations with explicit membranes and solvents to investigate the initial functional rotation process in AcrB driven by proton-motive force. Multiple MD simulations with different protonation states for Asp407 and Asp408 relates the specific protonation states and side-chain configurations. On the basis of the simulation results, we discuss proton translocation stoichiometry per the AcrB functional rotation cycle. Furthermore, conformational changes in the porter domain induced by modifying the TM-domain protonation states were analyzed.

■ METHODS

The crystal structure of the asymmetric AcrB trimer without drug molecules (PDB ID: 2DHH)[19] was used as the initial structure for the MD simulations herein. We modeled the missing portion of the crystal structure (residue number 499−512) using another crystal structure (PDB ID: 2J8S).[21] The AcrB trimer structure was embedded in an equilibrated lipid bilayer membrane with POPE (1-palmitoyl-2-oleoyl-sn-glycero-

3-phosphoethanolamine) using the following procedure. First, an initial pure POPE membrane was generated from a fully equilibrated POPC (1-palmitoyl-2-oleoyl-sn-glycero-3-phos-phocholine) membrane[41] and then equilibrated for 10-ns MD simulations. The TM region was estimated using the program TMHMM[42] and overlaid on the equilibrated POPE membrane, and we removed the lipid molecules for which the closest atomic distance from the protein was less than 1.5 Å. During this process, several threshold distances were used to remove lipid molecules. The threshold distance of 1.5 Å generated the smallest gap with no severe overlap between the protein and lipid molecules. A large hole with a diameter of ~30 Å in the TM center must be filled with phospholipids to avoid proton leakage across the membrane.[16] Twelve POPE molecules were manually packed into the hole (six for the upper leaflet and six for the lower leaflet). Next, the simulation box was filled with water molecules, and sodium ions were added as counterions. The system comprised ~470,000 atoms.

The simulations were performed with the MD program MARBLE[43] using CHARMM22/CMAP for the proteins,[44] CHARMM27 for the lipid molecules,[45] and TIP3P for water[46] as force-field parameters. Electrostatic interactions were calculated using the particle-mesh Ewald method.[47] The Lennard−Jones potential was smoothly switched to zero over the range of 8−10 Å. The symplectic integrator for rigid bodies was used to constrain the bond lengths and angles involving hydrogen atoms.[43] The time step was 2.0 fs. During the equilibration phase, the systems were gradually heated to 300 K for 1 ns with gradually lower position-harmonic restraints for the proteins; the systems were then equilibrated without restraints for 2 ns. The simulations were performed for the NPT ensemble through the extended-system method,[43,48] wherein the z axis corresponded to the membrane normal and was independently controlled, and the additional x and y axes were isotropically scaled.

Herein, we performed a series of MD simulations for the AcrB model, wherein we comprehensively changed the Asp407 and Asp408 protonation states in protomer E (Table 1). For the other titratable residues, we assumed the standard protonation states. The molecular figures were generated using PyMOL.[49]

Table 1. MD Simulations Summary

no.	Asp407[a]	Asp408[a]	initial structure	simulation time
1	−	−	X-ray	100 ns
2	−	H	X-ray	200 ns
3	H	−	X-ray	100 ns
4	H	H	X-ray	100 ns
5	−	−	2 at 100 ns	100 ns
6	−	−	2 at 50 ns	100 ns
7	−	−	X-ray	100 ns

[a]The protonation states of Asp407 and Asp408 in protomer E were changed. Asp407 and Asp408 in protomers A and B were deprotonated in each simulation. The aspartate deprotonated and protonated states are identified as "−" and "H", respectively.

Conformational changes in the porter domain were examined using principal component analysis (PCA). Snapshots of protomer E in the MD trajectories were aligned using a best fit for the TM domain (TM1:10−28, TM2:337−356, TM3:366−385, TM4:392−413, TM5:439−457, TM6:466−490, TM7:539−555, TM8:872−888, TM9:899−918,

TM10:925−943, TM11:973−992, and TM12:999−1018). Next, the variance−covariance matrix was calculated for the porter-domain Cα atoms of protomer E. The variance−covariance matrix was diagonalized to generate the principal component modes as eigenvectors. To avoid the effects from local motions in loops, only residues with a root-mean-square fluctuation in each subdomain less than 2.0 Å were used for this analysis. Therefore, in this PCA, we expected that the global motions of the porter domain relative to the TM domain were extracted. To quantitatively compare the PCA mode vectors and structural differences between the crystal structures, we employed the correlation coefficient, which is defined as follows:

$$C = \frac{\Delta \mathbf{a} \cdot \Delta \mathbf{b}}{|\Delta \mathbf{a}||\Delta \mathbf{b}|}$$

where $\Delta \mathbf{a}$ and $\Delta \mathbf{b}$ are the $3N$-dimensional atomic displacement vectors, and N is the number of atoms.

To complement the MD simulations, the pK_a values for Asp407, Asp408, and Lys940 in the crystal structure 2DHH were estimated using the programs PROPKA (versions 2.0 and 3.0)[50] and multi-conformation continuum electrostatics (MCCE).[51] PROPKA employs an empirical potential function that considers desolvation effects and intramolecular inter-actions. MCCE is based on the Poisson−Boltzmann equation combined with Monte Carlo sampling for the side-chain conformations and protonation states. Two different values for the protein dielectric constants were used (4.0 and 8.0) in MCCE.

■ RESULTS

We performed seven MD simulations for the AcrB trimer model, wherein the Asp407 and Asp408 protonation states in the TM domain were changed (Table 1). The root-mean-square deviations (RMSD) from the initial structures plateaued after ~30 ns for the individual domains and the full protein (Figure S1, Supporting Information). The TM domains were particularly stable, whereas the porter domains showed somewhat larger RMSD values, which support the porter-domain conformational changes described below. The number of contacts between the lipid molecules and TM domains rapidly plateaued during the equilibration phase at 3 ns (Figure S2, Supporting Information).

First, we examined a 100-ns MD simulation for the AcrB trimer model, wherein both Asp407 and Asp408 in the three protomers were deprotonated. This simulation is referred to as "simulation 1" (Table 1). Three distances from Lys940 Nζ to Asp407 Oδ, Asp408 Oδ, and Thr978 Oγ were used to indicate the side-chain arrangements for the four residues Lys940, Asp407, Asp408, and Thr978 (Figure 2).

For protomers A and B, throughout simulation 1, Lys940 formed stable salt bridges with both Asp407 and Asp408, and the distance between Lys940 and Thr978 was ~7 Å (Figures 3a and b), which shows that the side-chain configurations in the simulation are similar to the crystal structure (Figures 3a and b). This result indicates that both Asp407 and Asp408 are deprotonated in the A and B states. Therefore, for the MD simulations herein, both Asp407 and Asp408 were deproto-nated in protomers A and B.

In contrast to protomers A and B, the Lys940 side-chain configurations in protomer E exhibited dynamic behavior during simulation 1 (Figure 3c). During the first ~50 ns, Lys940 was located between Asp407 and Thr978, similar to
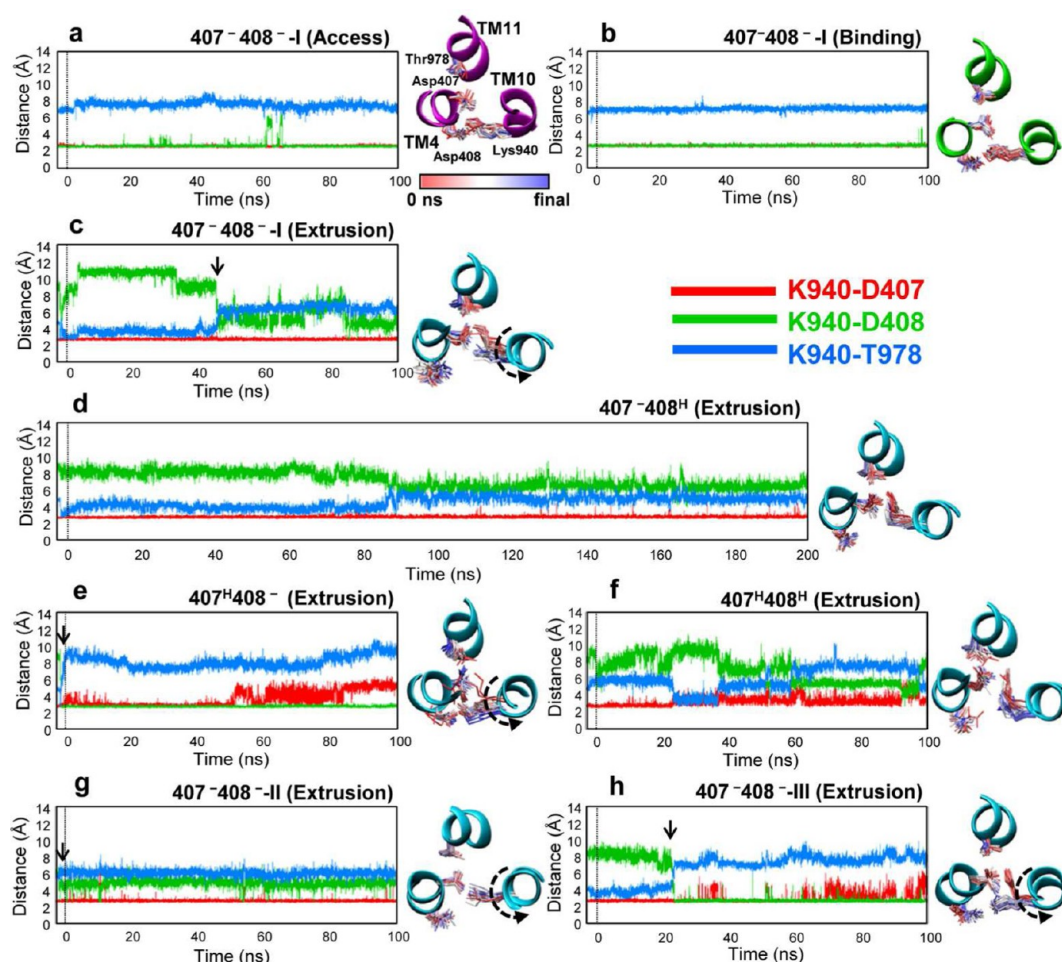
Figure 3. Asp407, Asp408, Lys940, and Thr978 side-chain configurations in the transmembrane domain. The time-dependent interatomic distances from Lys940 Nζ to Asp407 Oδ (red), Asp408 Oδ (green), and Thr978 Oγ (blue) are plotted. The side chain trajectories are shown for the initial (red) to final (blue) structures. Panels a, b, and c show the results for protomers A, B, and E in simulation 1 (D407⁻D408⁻), respectively. Panels d through h show the protomer E results from simulations 2 (D407⁻D408ᴴ), 3 (D407ᴴD408⁻), 4 (D407ᴴD408ᴴ), 5 (D407⁻D408⁻), and 6 (D407⁻D408⁻), respectively.

that in the crystal structure. However, at ~50 ns, the Lys940 side chain moved from Thr978 to Asp408, which is indicated with an arrow in Figure 3c. Though the Asp407 side chains rotated with the Lys940 shift, the interaction between Lys940 and Asp407 was retained throughout the simulation. When the Lys940 side chain moved, TM10 rotated relative to TM4 and TM11 (Figure 3c). For the final ~50 ns, Lys940 was located between Asp407 and Asp408, as shown in protomers A and B; however, the Lys940 and Asp408 salt bridge did not form completely. Consequently, deprotonation for both Asp407 and Asp408 destabilized the E-state side-chain configurations observed in the crystal structure. Thus, we next address the protonation state that stabilizes the E-state side-chain configurations.

We performed multiple MD simulations that comprehensively changed the Asp407 and Asp408 protonation states for protomer E. The simulation with Asp407 deprotonated and Asp408 protonated is referred to as "simulation 2" (Table 1). Likewise, the two simulations with only Asp408 deprotonated and both Asp407 and Asp408 protonated are referred to as "simulations 3 and 4", respectively (Table 1). Notably, Asp407 and Asp408 were deprotonated in each simulation for protomers A and B.

Throughout simulation 2 (D407⁻D408ᴴ indicates the Asp407 and Asp408 protonation states of protomer E for the readers' convenience), as shown in Figure 3d, Lys940 was closer to Thr978 than Asp408 for 200 ns. This side-chain configuration resembles the protomer-E configuration in the crystal structure, which indicates that Asp408 protonation stabilizes the E-state side-chain configuration. The slight increase in distance for Lys940-Thr978 (with a slight decrease in the Lys940-Asp408 distance) was observed at ~90 ns and was due to the interaction partner switching for the Lys940 amide group from one of the two Asp407 Oδ that directly interacts with Thr978 to the remaining Asp407 Oδ. Prior to switching, Lys940 formed hydrogen bonds either directly with Thr978 or via water mediation. At ~90 ns, another water molecule intercalated between the two residues, and Lys940 and Thr978 then interacted through one or two mediating water molecules.

In contrast to simulation 2 (D407⁻D408ᴴ), simulation 3 (D407ᴴD408⁻) showed that Lys940 immediately moved from Thr978 to Asp408 during the equilibration phase before the product run, which is indicated with an arrow in Figure 3e. Subsequently, Lys940 stably interacted with Asp407 and Asp408 for ~50 ns. However, the interaction between Lys940 and Asp407 was unstable for the final ~50 ns, but

Lys940 stably interacted with Asp408 throughout the simulation because the interaction between Lys940 and Asp407 was weaker due to the neutral, protonated Asp407. Therefore, Asp407 protonation and Asp408 deprotonation are incompatible with the E-state configuration.

In simulation 4 ($D407^H D408^H$), the Lys940 side chain exhibited dynamic behavior (Figure 3f). For the first ∼60 ns, Lys940 was closer to Thr978 than Asp408, and Lys940 formed a direct hydrogen bond with Thr978 from ∼20 to ∼40 ns. However, Lys940 moved from Thr978 to Asp408 at ∼60 ns then back to Thr978 at ∼90 ns. The interaction between Lys940 and Asp407 was somewhat unstable after ∼40 ns. Therefore, protonation of both Asp407 and Asp408 destabilizes the E-state configuration.

Summarizing the above simulation results, the combination with deprotonated Asp407 and protonated Asp408 is most compatible with the E-state side-chain configuration in the crystal structure.

To confirm the results, we performed two additional 100-ns MD simulations, wherein both Asp407 and Asp408 were deprotonated ("simulations 5 and 6") (Table 1). In simulation 5, a snapshot of simulation 2 ($D407^- D408^H$) at 100 ns was used as the initial structure, and simulation 6 began with a snapshot of simulation 2 ($D407^- D408^H$) at 50 ns. For these two snapshot structures, we changed the protonated Asp408 in protomer E to the deprotonated state, and each of the two snapshot structures was then simulated for an additional 100 ns. In simulation 5 ($D407^- D408^-$), Lys940 immediately shifted from Thr978 to Asp408 during the equilibration process and was between Asp407 and Asp408 for 100 ns (Figure 3g). In simulation 6 ($D407^- D408^-$), Lys940 similarly changed its position from Thr978 to Asp408 at ∼25 ns. Subsequently, Lys940 formed salt bridges with both Asp407 and Asp408 (Figure 3h). Therefore, both simulations 5 and 6 confirmed that Asp408 deprotonation generated Lys940 movement from Thr978 to Asp408.

To complement the MD simulations, we also estimated pK_a values for Asp407, Asp408, and Lys940 using the programs PROPKA and MCCE (Table 2). Both methods indicated that Asp407 and Asp408 in protomers A and B are deprotonated at pH 7. In protomer E, only Asp408 is protonated at pH 7. These results are consistent with our MD simulations.

Table 2. pK_a Simulations Summary

residues[a]	PROPKA		MCCE	
	v2.0	v3.0	$\varepsilon_p = 4$[b]	$\varepsilon_p = 8$[b]
Asp407 (A)	4.52	3.88	<0	<0
(B)	5.24	4.07	<0	<0
(E)	4.91	6.57	0.76 ± 0.07	1.20 ± 0.05
Asp408 (A)	3.32	5.41	6.95 ± 0.18	4.89 ± 0.12
(B)	3.28	5.89	6.32 ± 0.32	5.01 ± 0.07
(E)	7.10	8.77	9.88 ± 0.12	7.06 ± 0.07
Lys940 (A)	11.44	12.20	>14	>14
(B)	11.26	11.95	>14	>14
(E)	8.51	8.89	>14	>14

[a](A), (B) and (E) are protomers A, B, and E in the AcrB trimer, respectively. [b]In MCCE, two different protein dielectric constants were used. For each dielectric constant, the pK_a value averages and standard errors were estimated through ten independent calculations with different random numbers.

Next, we examined structural changes in the porter domain during the simulations. We expected that changing the TM-domain protonation state induces structural changes in the porter domain. Despite the short time scale for the all-atom MD simulations, the initial structural change processes for the porter domain were shown in our simulations. Because Asp408 in protomer E was deprotonated in simulation 1, we expected that protomer E in simulation 1 would undergo a structural transition from state E to A. Therefore, global motions for the porter domain in protomer E relative to the TM domain in simulation 1 were examined using PCA. The first and second PCA modes accounted for 90% and 4% of the total motions, respectively, which indicates that the first mode dominates the porter-domain motions. The average projection for the final 1-ns structures in protomer E onto a plane with modes 1 and 2 was similar to protomer A of the crystal structure, suggesting that the porter domain of protomer E underwent a structural transition from state E to A (Figure 4a). Mode 1 was a rotational motion around PC1 (Figures 4c to f), and the correlation coefficient between the mode-1 vector and structural difference in the crystal structure for the E and A protomers was 0.74. In contrast, mode 2 was a breathing motion outward and inward along a line connecting PN1 and PC1 (Figure 4b). Here, we used the starting structure as the reference structure for PCA because we aimed to examine structural transitions during MD simulations from the starting structure. The PCA results do not strongly depend on the reference structure. Conventionally for PCA, the average structure is used as the reference structure. For comparison, conventional PCA was also performed using the average structures for both the TM and porter domains as the reference structures. The resulting twisting motions between the TM and porter domains were observed as mode-1 motions (Figure S3, Supporting Information), which is consistent with the above PCA results, wherein the TM domain crystal structure was used as the reference structure. Because the structural transition from the crystal structure and the relative TM and porter domain motions are important herein, only the TM domain was used for fitting, and PCA was performed for the porter domain.

Motions of the drug exit and entrance related to alternating access of drugs during simulation 1 were examined. In protomer E, the drug exit is between PN1 and PN2. In protomer E of the crystal structure, the α-helix Nα2, which was in the trimer center, is inclined, blocks the protomer-B drug exit and opens the protomer-E drug exit. In contrast, for protomers A and B, α-helix Nα2 stands approximately perpendicular to the membrane. Therefore, the inclined α-helix Nα2 is a special feature of the protomer E of the crystal structure. During simulation 1, the α-helix Nα2 tilt in protomer E was reduced, as shown in mode 1 (Figure 4c), which is consistent with the structural changes from the E to A state. The correlation coefficient between PN1 mode-1 vector and the PN1 structural differences in the crystal structure for protomers E and A was 0.89. The structural changes in the porter domain during simulation 1 appear as a step in the AcrB functional rotation.

The drug entrance is between PC2 and TM. The crystal structure shows structural changes in the region that connects PC2 and TM8 for protomers E and A (Figure 4e). In protomer E, α-helix TM8 is extended to the periplasmic side, and the drug entrance is closed. In contrast, the periplasmic extension of α-helix TM8 for protomers A and B is unwound, and the drug entrance is in the vicinity of the unwound loop.
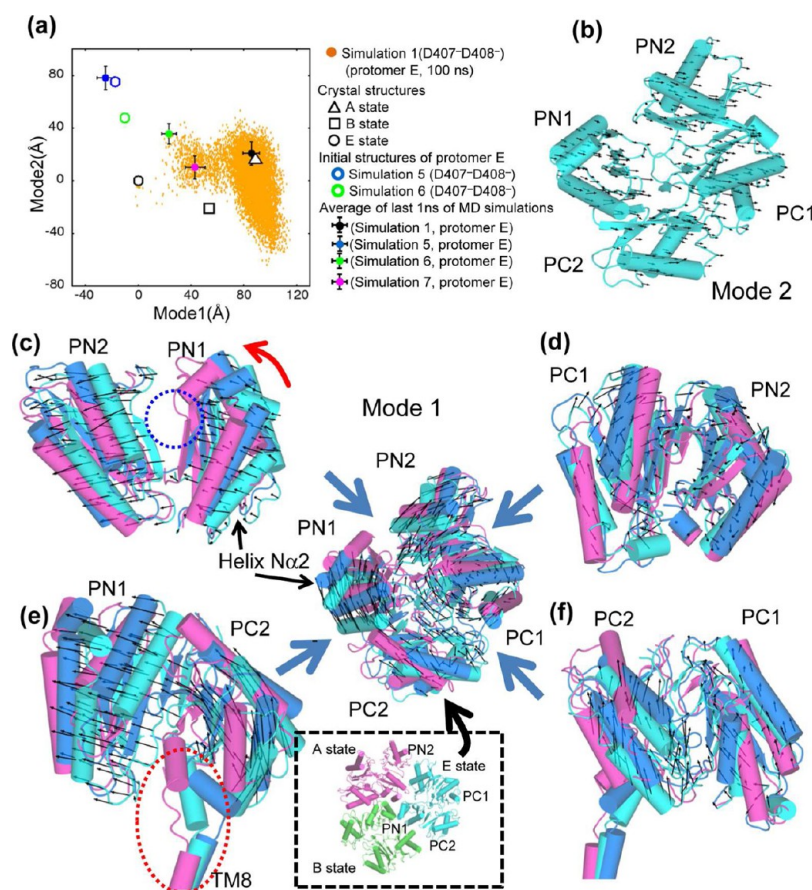
Figure 4. PCA results for the porter domain of protomer E from simulation 1 (D407⁻D408⁻). Panel a shows snapshot projections onto modes 1 and 2, as well as the crystal-structure (protomers A, B, and E) projections. The average projection of the last 1-ns structures is similar to protomer A. In panel b, the second mode directions (black arrows) are shown in the protomer-E porter domain (cyan) from the crystal structure. In panels c−f, the first mode directions are shown using black arrows. For comparison, the protomers E (cyan) and A (magenta) of the crystal structure and final simulation 1 structure (blue) are also shown. The structures were aligned using least-squares fits of the TM domain. In the central panel, the top view of the porter domain is shown. Side views for the subdomain pairs PN1-PN2, PN1-PC2, PC1-PN2, and PC1-PC2 are shown in panels c, d, e, and f, respectively. The direction of the α-helix Nα2 conformational changes during the simulation is indicated with a red arrow (c). The drug exit is between PN1 and PN2 (c, blue circle). The drug entrance is near the upper portion of TM8 (e, red oval). The upper portion of TM8 in the final structure from simulation 1 (D407⁻D408⁻) is also shown (e and f, blue cylinder).

Simulation 1 showed that the TM8 periplasmic extension was unwound in protomer E; however, the residual α-helix location differed somewhat from the crystal structure position (Figure 4e). Because of the different residual α-helix locations, the drug entrance for the final structure in simulation 1 is smaller than that for the crystal structure. The cleft between PC1 and PC2 has been proposed as another drug entrance.[21] The cleft is open in the protomers A and B of the crystal structure, while it is closed in protomer E. However, the cleft is regarded as an AcrA binding site, and structural changes in the porter domain may be transmitted to TolC through the cleft and AcrA. In simulation 1, the cleft in protomer E was not open, but PC2 moved upward and maintained contact with PC1 (Figure 4f). The discrepancy in PC2 movement is likely due to insufficient sampling and/or the absence of AcrA in the simulation. In contrast to PN1, PN2, and PC2, the PC1 structural transition was small during simulation 1, which is consistent with the crystal structure (Figure 4d).

Summarizing the above results of simulation 1, the porter domain showed a clear trend of structural transitions from the E to A state, consistent with the side-chain configuration change in the TM domain.

In simulation 2, we expected that the porter domain retained its initial conformation in protomer E because the side-chain configurations in the corresponding TM domain remained similar to those of the crystal structure due to Asp408 protonation. Mode 1 in simulation 2 (D407⁻D408ᴴ) is a translational motion outward from PC1 and PC2 (Figure 5a) and resembles the mode 2 outward motions in simulation 1 (Figure 4b). As described above, AcrA may bind at the cleft between PC1 and PC2. The translational motions outward from PC1 and PC2 are likely due to the absence of AcrA in our simulations. In contrast to simulation 1, the tilt was retained for α-helix Nα2, which is near the protomer-E drug exit. At the drug entrance, the α-helix TM8 periplasmic extension was also retained. The correlation coefficient between the mode-1 vector for simulation 2 and the E-A crystal structure difference is only −0.20, which indicates that the porter-domain motion in simulation 2 clearly differs from the E-A structural change in the crystal structure.

Considering the different porter domain behaviors in simulations 1 and 2, Asp408 deprotonation for the simulation-2 snapshots may induce the conformational changes as observed in simulation 1. Therefore, we examined the additional simulations 5 and 6 for both the deprotonated
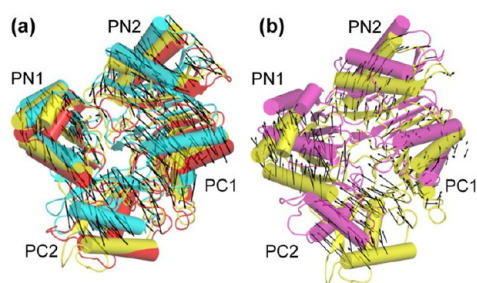
Figure 5. PCA results for the porter domain of protomer E from simulations 2 (D407⁻D408ᴴ) and 6 (D407⁻D408⁻). Panel a shows the directions for the first mode in simulation 2 (black arrows), the porter-domain structures at 50 ns (yellow) and 100 ns (red) from simulation 2, and the protomer-E crystal structure (cyan). The 50-ns and 100-ns structures from simulation 2 were the initial structures of simulations 5 and 6, respectively. In panel b, the first mode directions in simulation 6 are shown with black arrows. For comparison, the crystal-structure of protomer A (magenta) and the simulation 6 initial structure (yellow) are also shown. The structures were aligned using least-squares fits for the TM domain.

Asp407 and Asp408, which began with snapshots from simulation 2. Simulations 5 and 6 showed different behaviors from each other. In simulation 5, the structures remained similar to the initial structure, which suggests that the structure could not escape the free-energy basin of the starting structure, which was the 100-ns snapshot in simulation 2 (Figure 4a). In contrast, simulation 6 that began with the snapshot at 50 ns showed the trend for the structural transition from states E to A (Figure 4a), though the porter domain did not fully reach the A-state structure. Mode 1 of simulation 6 is a rotational motion around PC1, which also resembles the structural transition from state E to A (Figure 5b).

Additionally, to improve our statistics, we performed another 100-ns MD simulation under the same conditions as simulation 1, except for the initial velocities (simulation 7, Figure S4, Supporting Information). Mode 1 of simulation 7 also showed the rotational motion around PC1 that was observed in simulations 1 and 6 (Figures S4, Supporting Information). The mode-1 correlation coefficient between simulations 1 and 7 was 0.70. These results indicate that Asp408 deprotonation induced the porter-domain conformational changes from the E to A states, though the conformational changes are likely transmitted stochastically.

In addition to conformational changes in protomer E, the asymmetric coupling between the trimer protomers was also examined. The Nα2 helices in the timer center are the asymmetric features of AcrB (Figure S5, Supporting Information). The Nα2 helices from different protomers are proximal to one another, and only the protomer-E Nα2 helix is considerably inclined. The distances between Gln112 Cα atoms for the different protomers are good indicators for the Nα2 helix asymmetric arrangements (Figure S5, Supporting Information). Interestingly, the three distances between protomers E-A, E-B, and A-B in simulation 1 converged into a single value (Figure S6, Supporting Information), which suggests that the trimer transitioned to an approximately symmetric structure during simulation 1. In contrast, asymmetric protonation states were applied in simulation 2, and the asymmetric features of the Nα2 helices were retained (Figure S6, Supporting Information). The PCA for protomer B in simulation 1 also indicated a trend wherein the structure

transitioned from the B to A state, whereas protomer A retained its A-state conformation (Figure S7, Supporting Information). Therefore, the simulation-1 timer transitions to the symmetric "AAA" state. The first crystal structure solved in 2002[16] shows a symmetric trimer, and the protomer conformation in the first crystal structure resembles the A state in its asymmetric structure (i.e., the first crystal structure is in the "AAA" state). The trend wherein the structure transitions to a symmetric structure is reasonable because the protonation states are the same for the three protomers in simulation 1. The "AAA" symmetric conformation is one possible conformation for AcrB, which likely corresponds to a resting state.

■ DISCUSSION

Herein, we performed multiple MD simulations involving the asymmetrical AcrB trimer model, wherein the Asp407 and Asp408 protonation states in protomer E were changed. The results indicate that the Asp408 protonation state is critically important for retaining the side-chain configurations in the TM domain. Experiments using dicyclohexylcarbodiimide (DCCD), which reacts to amino acids with a protonated carboxylic acid, suggested that Asp408 was protonated.[29] The experiments showed that the apparent pK_a for Asp408 was 7.4, which would facilitate proton binding and release under physiological conditions. The results from our MD simulations are consistent with the experimental results. A recent MD-simulation study by Fischer and Kandt[30] also supports our result; they used protonated Asp408 for protomer A, which differs from the conditions herein. Their simulation showed Lys940 movement in protomer A to a configuration that resembled protomer E. However, the structural transition was opposite to the AcrB functional rotation proposed previously.[19−21] Nevertheless, both their simulation and the MD simulation herein suggest that Asp408 protonation is key for side-chain configuration changes from the A or B to E state.

The Asp407 protonation state also affects the Lys940 side-chain dynamics. In simulations 3 and 4 with protonated Asp407, the Lys940 side-chain configurations were unstable because the neutral, protonated Asp407 weakened the interaction between Lys940 and Asp407. The asymmetric AcrB trimer crystal structure showed a direct interaction between Lys940 and Asp407 for the A, B, and E protomers (Figure 2). Experimental studies have suggested that this interaction is important. The D407A, D407N, or D407E mutation substantially decreased function.[27−29] The D407A and D407N mutations indicated that a carboxylic group in Asp407 is indispensable for function. Despite the retention of a carboxylic group in the D407E mutation, the AcrB activity substantially decreased upon mutation likely due to the different side-chain lengths between the aspartate and glutamate. The glutamate side chain is longer than aspartate by one carbon atom. Therefore, the D407E mutant of the Lys940 and Glu407 side chains did not fit between TM4 and TM10. Although our simulation suggests that Asp407 protonation is incompatible with the A-, B-, and E-state configurations, the possibility of transient protonation of Asp407 during proton translocation cannot be ruled out. In contrast to Asp407, the D408E mutation retains substantial activity, whereas the D408A and D408N mutants completely lose function,[27] which suggests that a carboxylic group in residue 408 is indispensable to AcrB function.

Lys940 may also be deprotonated during proton translocation. Considering the direct interaction between Lys940
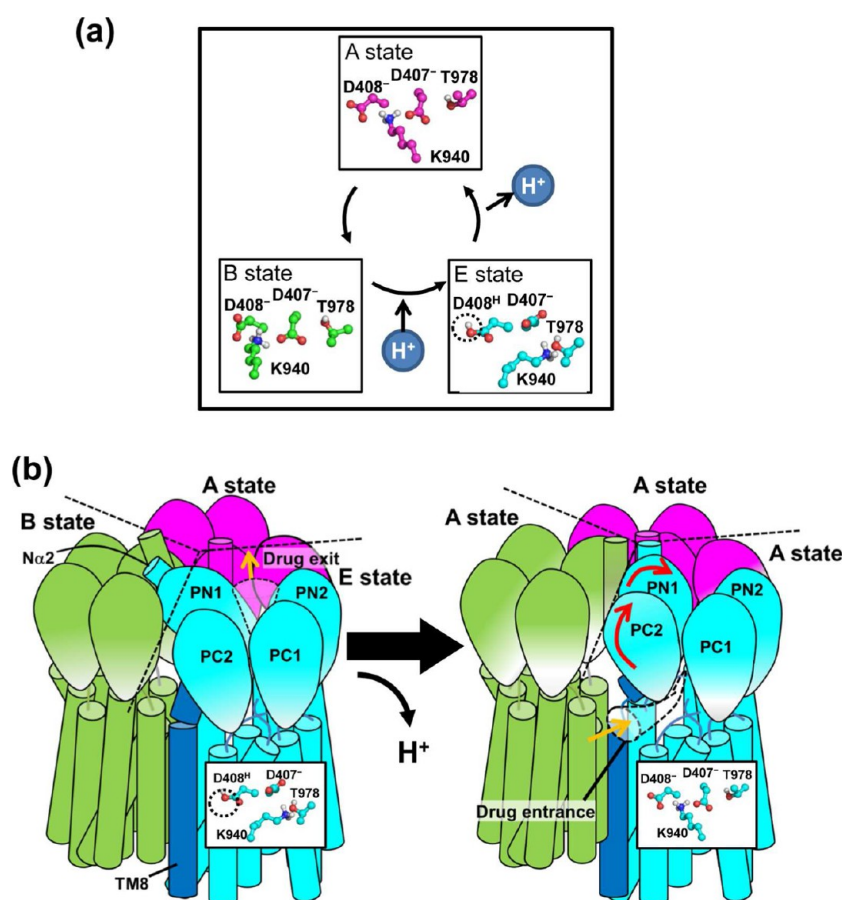
Figure 6. AcrB protonation cycle and conformational changes followed by proton dissociation. Panel a shows the proposed AcrB protonation cycle. In the A and B states, both Asp407 and Asp408 are deprotonated, whereas only Asp408 is protonated in the E state. From the B to E state, the proton binds, and from the E to A state, the proton dissociates from Asp408. Panel b summarizes conformational changes in the porter domain during our simulations. Following proton dissociation from the TM domain in protomer E, the porter domain rotates (red arrows), which closes the drug exit and opens the drug entrance. The central Nα2 helices undergo transitions from the asymmetric to symmetric arrangement, and the final structure resembles the symmetric "AAA" structure, which likely corresponds to the resting state. The drug movement directions are indicated with orange arrows. For clarity, the TolC docking domains are not shown in panel b.

and Asp407 in each protomer (A, B, and E) when Lys940 is deprotonated, Asp407 might become protonated. However, the pK_a calculations suggest that Lys940 is not deprotonated at pH 7 (Table 2). The possibility of the transient deprotonation of Lys940 during proton translocation also cannot be excluded.[29]

The T978A mutation was reported to decrease AcrB activity to 8%.[28] However, the T978S mutation retained 77% of the wild-type activity. In our simulations with protonated Asp408, the Thr978 and Lys940 side chains in protomer E either directly interacted with or formed a water-mediated hydrogen bond. This result suggests that Thr978 side-chain hydrogen bonding is critical for E-state configuration stability, which is consistent with the mutation experiment.

The proton translocation stoichiometry is important for elucidating the AcrB drug export mechanism. Considering the direct interaction between Asp407 and Lys940 in each protomer, Asp407 and Lys940 are likely always charged. Even if Asp407 is protonated, Lys940 is deprotonated in this case. Our simulations indicate that deprotonation of only Asp408 induces a structural transition for Lys940 from the E to A state. Thus, these results suggest that proton translocation stoichiometry may be one proton per complete cycle of one AcrB protomer (Figure 6a). In the trimer, the proton translocation stoichiometry may be one proton per step

(120° rotation), when a cyclic transition is assumed (i.e., "ABE", "BEA" to "EAB").

Despite the short time scale for all-atom MD simulations, the simulation with both Asp407 and Asp408 deprotonated showed that the porter domain structure transitioned from a protomer-E to protomer-A-like structure. Here, we discuss the transmission pathway for structural changes from the TM to the porter domain. When Asp408 was deprotonated, TM4, which includes Asp407 and Asp408, undergoes a twisting motion relative to TM10. On the periplasmic side of the TM domain, a long loop connects TM1 and PN1 and mediates interactions between loop TM3-TM4 and PN2. The TM4 twisting may influence the PN1 and PN2 movements through these loops. In a pseudo 2-fold symmetrical manner, a long loop connects TM7 and PC1, which is located between loop TM9-TM10 and PC2 and is adjacent to the upper portion of TM8. The TM10 twisting motion may affect unwinding in the upper portion of TM8 through these loops. In addition, a water entrance connected to the TM domain center is located between TM9 and TM10.[30] The water accessibility may affect unwinding of the upper portion of TM8.

It is also interesting that proton binding and dissociation in each protomer are coupled to this reaction in the remaining protomers. Because contacts between different protomer TM

domains are few, proton binding and dissociation may not be directly coupled with the other protomers through the TM domains. The many porter domain contacts between different protomers suggest that it may be the site for coupling. Moreover, previous coarse-grained simulations[39] have shown that conformational changes in the porter domain of one protomer influences other protomers; the simulations suggest that drug dissociation from protomer B in an asymmetric BEA structure likely generates the symmetric AAA structure. In our simulations, without drug molecules bound, when the TM-domain protonation states were not uniform, the asymmetric structure was retained. In contrast, when the TM-domain protonation states were uniform, the asymmetric structure showed a trend wherein it transitions to the symmetric AAA structure (i.e., a potential resting state), which indicates that the asymmetric structure is generated by the TM-domain protonation states and drug binding (Figure 6b).

Because the time scale for the MD simulations herein is limited to ∼100 ns, the long-distance coupling mechanism for the conformational changes may be hypothetical. For conclusive results, more extensive MD simulations and/or free-energy simulations are necessary.

CONCLUSIONS

We have performed unbiased all-atom MD simulations for the asymmetric AcrB with explicit membranes and water to investigate the aspartate protonation states in the TM domain, which likely play a crucial role in proton translocation. In protomers A and B, both Asp407 and Asp408 are deprotonated and form stable salt bridges with Lys940 throughout our simulations. We performed MD simulations, wherein we comprehensively changed the Asp407 and Asp408 protonation states for protomer E. Deprotonated Asp407 and protonated Asp408 were most compatible with the E-state side-chain configuration. For the two additional MD simulations with deprotonated Asp408, we began with two snapshots from the simulation with protonated Asp408 and observed spontaneous structural shifts for Lys940 in protomer E. These results suggest that the proton translocation stoichiometry may be one proton per complete cycle of one AcrB protomer. In the trimer, the proton translocation stoichiometry may be one proton per step (120° rotation) when we assume cyclic transitions (i.e., "ABE", "BEA" to "EAB"). Our simulations suggest that Asp408 protonation is important, which is consistent with additional experimental and simulation results.

The next question is whether the protonation-state changes in the transmembrane domain induce large conformational changes in the porter domain, which are primarily responsible for drug export. Despite the limited time scale for conventional MD simulations, we observed conformational change processes in the porter domain through our simulations. Two functional AcrB rotations (the conformational changes in the TM and porter domains) appear coupled in the simulation. However, to observe the full transition between such states and to elucidate the molecular mechanism underlying drug export, more extensive simulations and/or free-energy experiments, such as umbrella sampling, are necessary. We are currently undertaking such studies.

ASSOCIATED CONTENT

ⓢ Supporting Information

Series of Cα root mean square deviations (RMSD) for simulations 1−7 (Figure S1); time courses for the number of contacts between the trimer TM domain and POPE molecules (Figure S2); PCA Results for which the average structure of the TM and porter domains was used as the reference structure (Figure S3); results from simulation 7 (Figure S4); the Nα2 helix arrangements in the A, B, and E protomers (Figure S5); time-dependent inter-atomic distances between Gln112 Cα atoms in different protomers (Figure S6); and PCA results for porter-domain conformational changes in protomers A and B from simulation 1 (Figure S7). This material is available free of charge via the Internet at http://pubs.acs.org.

AUTHOR INFORMATION

Corresponding Author

*E-mail: ike@tsurumi.yokohama-cu.ac.jp. Tel: +81-45-508-7232.

Notes

The authors declare no competing financial interest.

ABBREVIATIONS

AcrB, acriflavine resistance protein B; AcrA, acriflavine resistance protein A; RND, resistance, nodulation, and cell division; POPE, 1-palmitoyl-2-oleoyl-*sn*-glycero-3-phosphoethanolamine; DCCD, dicyclohexylcarbodiimide; MD, molecular dynamics; TM, transmembrane; PCA, principal component analysis; RMSD, root-mean-square deviation

REFERENCES

(1) Li, X. Z., and Nikaido, H. (2004) Efflux-mediated drug resistance in bacteria. *Drugs 64*, 159−204.
(2) Poole, K., Krebes, K., McNally, C., and Neshat, S. (1993) Multiple antibiotic resistance in Pseudomonas aeruginosa: evidence for involvement of an efflux operon. *J. Bacteriol. 175*, 7363−7372.
(3) Poole, K. (2001) Multidrug resistance in Gram-negative bacteria. *Curr. Opin. Microbiol. 4*, 500−508.
(4) Ma, D., Cook, D. N., Hearst, J. E., and Nikaido, H. (1994) Efflux pumps and drug resistance in gram-negative bacteria. *Trends Microbiol. 2*, 489−493.
(5) Okusu, H., Ma, D., and Nikaido, H. (1996) AcrAB efflux pump plays a major role in the antibiotic resistance phenotype of Escherichia coli multiple-antibiotic-resistance (Mar) mutants. *J. Bacteriol. 178*, 306−308.
(6) Dinh, T., Paulsen, I. T., and Saier, M. H., Jr. (1994) A family of extracytoplasmic proteins that allow transport of large molecules across the outer membranes of gram-negative bacteria. *J. Bacteriol. 176*, 3825−3831.
(7) Paulsen, I. T., Park, J. H., Choi, P. S., and Saier, M. H., Jr. (1997) A family of gram-negative bacterial outer membrane factors that

function in the export of proteins, carbohydrates, drugs and heavy metals from gram-negative bacteria. *FEMS Microbiol. Lett. 156*, 1−8.

(8) Tikhonova, E. B., and Zgurskaya, H. I. (2004) AcrA, AcrB, and TolC of *Escherichia coli* form a stable intermembrane multidrug efflux complex. *J. Biol. Chem. 279*, 32116−32124.

(9) Tamura, N., Murakami, S., Oyama, Y., Ishiguro, M., and Yamaguchi, A. (2005) Direct interaction of multidrug efflux transporter AcrB and outer membrane channel TolC detected via site-directed disulfide cross-linking. *Biochemistry 44*, 11115−11121.

(10) Sulavik, M. C., Houseweart, C., Cramer, C., Jiwani, N., Murgolo, N., Greene, J., DiDomenico, B., Shaw, K. J., Miller, G. H., Hare, R., and Shimer, G. (2001) Antibiotic susceptibility profiles of Escherichia coli strains lacking multidrug efflux pump genes. *Antimicrob. Agents Chemother. 45*, 1126−1136.

(11) Zgurskaya, H. I., and Nikaido, H. (1999) Bypassing the periplasm: reconstitution of the AcrAB multidrug efflux pump of *Escherichia coli. Proc. Natl. Acad. Sci. U.S.A. 96*, 7190−7195.

(12) Koronakis, V., Sharff, A., Koronakis, E., Luisi, B., and Hughes, C. (2000) Crystal structure of the bacterial membrane protein TolC central to multidrug efflux and protein export. *Nature 405*, 914−919.

(13) Eswaran, J., Koronakis, E., Higgins, M. K., Hughes, C., and Koronakis, V. (2004) Three's company: component structures bring a closer view of tripartite drug efflux pumps. *Curr. Opin. Struct. Biol. 14*, 741−747.

(14) Mikolosko, J., Bobyk, K., Zgurskaya, H. I., and Ghosh, P. (2006) Conformational flexibility in the multidrug efflux system protein AcrA. *Structure 14*, 577−587.

(15) Zgurskaya, H. I., and Nikaido, H. (2000) Multidrug resistance mechanisms: drug efflux across two membranes. *Mol. Microbiol. 37*, 219−225.

(16) Murakami, S., Nakashima, R., Yamashita, E., and Yamaguchi, A. (2002) Crystal structure of bacterial multidrug efflux transporter AcrB. *Nature 419*, 587−593.

(17) Murakami, S., and Yamaguchi, A. (2003) Multidrug-exporting secondary transporters. *Curr. Opin. Struct. Biol. 13*, 443−452.

(18) Lomovskaya, O., Zgurskaya, H. I., and Nikaido, H. (2002) It takes three to tango. *Nat. Biotechnol. 20*, 1210−1212.

(19) Murakami, S., Nakashima, R., Yamashita, E., Matsumoto, T., and Yamaguchi, A. (2006) Crystal structures of a multidrug transporter reveal a functionally rotating mechanism. *Nature 443*, 173−179.

(20) Seeger, M. A., Schiefner, A., Eicher, T., Verrey, F., Diederichs, K., and Pos, K. M. (2006) Structural asymmetry of AcrB trimer suggests a peristaltic pump mechanism. *Science 313*, 1295−1298.

(21) Sennhauser, G., Amstutz, P., Briand, C., Storchenegger, O., and Grutter, M. G. (2007) Drug export pathway of multidrug exporter AcrB revealed by DARPin inhibitors. *PLoS Biol. 5*, e7.

(22) Jardetzky, O. (1966) Simple allosteric model for membrane pumps. *Nature 211*, 969−970.

(23) Forrest, L. R., Kramer, R., and Ziegler, C. (2011) The structural basis of secondary active transport mechanisms. *Biochim. Biophys. Acta 1807*, 167−188.

(24) Al-Shawi, M. K. (2011) Catalytic and transport cycles of ABC exporters. *Essays Biochem. 50*, 63−83.

(25) Weyand, S., Shimamura, T., Beckstein, O., Sansom, M. S., Iwata, S., Henderson, P. J., and Cameron, A. D. (2011) The alternating access mechanism of transport as observed in the sodium-hydantoin transporter Mhp1. *J. Synchrotron Radiat. 18*, 20−23.

(26) Murakami, S. (2008) Multidrug efflux transporter, AcrB–the pumping mechanism. *Curr. Opin. Struct. Biol. 18*, 459−465.

(27) Guan, L., and Nakae, T. (2001) Identification of essential charged residues in transmembrane segments of the multidrug transporter MexB of *Pseudomonas aeruginosa. J. Bacteriol. 183*, 1734−1739.

(28) Takatsuka, Y., and Nikaido, H. (2006) Threonine-978 in the transmembrane segment of the multidrug efflux pump AcrB of *Escherichia coli* is crucial for drug transport as a probable component of the proton relay network. *J. Bacteriol. 188*, 7284−7289.

(29) Seeger, M. A., von Ballmoos, C., Verrey, F., and Pos, K. M. (2009) Crucial role of Asp408 in the proton translocation pathway of multidrug transporter AcrB: evidence from site-directed mutagenesis and carbodiimide labeling. *Biochemistry 48*, 5801−5812.

(30) Fischer, N., and Kandt, C. (2011) Three ways in, one way out: water dynamics in the trans-membrane domains of the inner membrane translocase AcrB. *Proteins 79*, 2871−2885.

(31) Eicher, T., Cha, H. J., Seeger, M. A., Brandstatter, L., El-Delik, J., Bohnert, J. A., Kern, W. V., Verrey, F., Grutter, M. G., Diederichs, K., and Pos, K. M. (2012) Transport of drugs by the multidrug transporter AcrB involves an access and a deep binding pocket that are separated by a switch-loop. *Proc. Natl. Acad. Sci. U.S.A. 109*, 5687−5692.

(32) Schulz, R., Vargiu, A. V., Collu, F., Kleinekathofer, U., and Ruggerone, P. (2010) Functional rotation of the transporter AcrB: insights into drug extrusion from simulations. *PLoS Comput. Biol. 6*, e1000806.

(33) Vargiu, A. V., Collu, F., Schulz, R., Pos, K. M., Zacharias, M., Kleinekathofer, U., and Ruggerone, P. (2011) Effect of the F610A mutation on substrate extrusion in the AcrB transporter: explanation and rationale by molecular dynamics simulations. *J. Am. Chem. Soc. 133*, 10704−10707.

(34) Schulz, R., Vargiu, A. V., Ruggerone, P., and Kleinekathofer, U. (2011) Role of water during the extrusion of substrates by the efflux transporter AcrB. *J. Phys. Chem. B 115*, 8278−8287.

(35) Fischer, N., and Kandt, C. (2013) Porter domain opening and closing motions in the multi-drug efflux transporter AcrB. *Biochim. Biophys. Acta 1828*, 632−641.

(36) Feng, Z., Hou, T., and Li, Y. (2012) Unidirectional peristaltic movement in multisite drug binding pockets of AcrB from molecular dynamics simulations. *Mol. Biosyst. 8*, 2699−2709.

(37) Takatsuka, Y., Chen, C., and Nikaido, H. (2010) Mechanism of recognition of compounds of diverse structures by the multidrug efflux pump AcrB of *Escherichia coli. Proc. Natl. Acad. Sci. U.S.A. 107*, 6559−6565.

(38) Vargiu, A. V., and Nikaido, H. (2012) Multidrug binding properties of the AcrB efflux pump characterized by molecular dynamics simulations. *Proc. Natl. Acad. Sci. U.S.A. 109*, 20637−20642.

(39) Yao, X. Q., Kenzaki, H., Murakami, S., and Takada, S. (2010) Drug export and allosteric coupling in a multidrug transporter revealed by molecular simulations. *Nat. Commun. 1*, 117.

(40) Lu, W. C., Wang, C. Z., Yu, E. W., and Ho, K. M. (2006) Dynamics of the trimeric AcrB transporter protein inferred from a B-factor analysis of the crystal structure. *Proteins 62*, 152−158.

(41) Hashido, M., Kidera, A., and Ikeguchi, M. (2007) Water transport in aquaporins: osmotic permeability matrix analysis of molecular dynamics simulations. *Biophys. J. 93*, 373−385.

(42) Sonnhammer, E. L., von Heijne, G., and Krogh, A. (1998) A Hidden Markov Model for Predicting Transmembrane Helices in Protein Sequences, in *Proceedings of the Sixth International Conferance on Intelligent Systems for Molecular Biology* (Glasgow, T. L., Major, F., Lathrop, R., Sankoff, D., and Sensen, C., Eds.), pp 175−182, AAAI Press, Menlo Park, CA.

(43) Ikeguchi, M. (2004) Partial rigid-body dynamics in NPT, NPAT and NPgammaT ensembles for proteins and membranes. *J. Comput. Chem. 25*, 529−541.

(44) Mackerell, A. D., Jr., Feig, M., and Brooks, C. L., III (2004) Extending the treatment of backbone energetics in protein force fields: limitations of gas-phase quantum mechanics in reproducing protein conformational distributions in molecular dynamics simulations. *J. Comput. Chem. 25*, 1400−1415.

(45) Feller, S. E., and MacKerell, A. D. (2000) An improved empirical potential energy function for molecular simulations of phospholipids. *J. Phys. Chem. B 104*, 7510−7515.

(46) Jorgensen, W. (1983) Comparison of simple potential functions for simulating liquid water. *J. Chem. Phys. 79*, 926.

(47) Essmann, U. (1995) A smooth particle mesh Ewald method. *J. Chem. Phys. 103*, 8577.

(48) Martyna, G. J., Tobias, D. J., and Klein, M. L. (1994) Constant pressure molecular dynamics algorithms. *J. Chem. Phys. 101*, 4177.

(49) *The PyMOL Molecular Graphics System*, Version 1.5.0.3, Schrodinger, LLC..

(50) Li, H., Robertson, A. D., and Jensen, J. H. (2005) Very fast empirical prediction and rationalization of protein pKa values. *Proteins* 61, 704–721.

(51) Song, Y., Mao, J., and Gunner, M. R. (2009) MCCE2: improving protein pKa calculations with extensive side chain rotamer sampling. *J. Comput. Chem. 30*, 2231–2247.